The Munc18-1 domain 3a hinge-loop controls syntaxin-1A nanodomain assembly and engagement with the SNARE complex during secretory vesicle priming

Ravikiran Kasula,[1] Ye Jin Chai,[1] Adekunle T. Bademosi,[1] Callista B. Harper,[1] Rachel S. Gormal,[1] Isabel C. Morrow,[1,2] Eric Hosy,[4,5] Brett M. Collins,[3] Daniel Choquet,[4,5,6] Andreas Papadopulos,[1] and Frédéric A. Meunier[1]

[1]Queensland Brain Institute, Clem Jones Centre for Ageing Dementia Research, [2]Australian Institute for Bioengineering and Nanotechnology, and [3]Institute for Molecular Bioscience, The University of Queensland, Brisbane, Queensland 4072, Australia
[4]Interdisciplinary Institute for Neuroscience, University of Bordeaux, 33077 Bordeaux, France
[5]Centre National de la Recherche Scientifique, Unité Mixte de Recherche 5297, 33077 Bordeaux, France
[6]Bordeaux Imaging Center, Unité Mixte de Service 3420, Centre National de la Recherche Scientifique, US4 Institut National de la Santé et de la Recherche Médicale, University of Bordeaux, 33077 Bordeaux, France

Munc18-1 and syntaxin-1A control SNARE-dependent neuroexocytosis and are organized in nanodomains on the plasma membrane of neurons and neurosecretory cells. Deciphering the intra- and intermolecular steps via which they prepare secretory vesicles (SVs) for fusion is key to understanding neuronal and hormonal communication. Here, we demonstrate that expression of a priming-deficient mutant lacking 17 residues of the domain 3a hinge-loop (Munc18-1$^{\Delta317\text{-}333}$) in PC12 cells engineered to knockdown Munc18-1/2 markedly prolonged SV docking. Single-molecule analysis revealed nonhomogeneous diffusion of Munc18-1 and syntaxin-1A in and out of partially overlapping nanodomains. Whereas Munc18-1^{WT} mobility increased in response to stimulation, syntaxin-1A became less mobile. These Munc18-1 and syntaxin-1A diffusional switches were blocked by the expression of Munc18-1$^{\Delta317\text{-}333}$, suggesting that a conformational change in the Munc18-1 hinge-loop controls syntaxin-1A and subsequent SNARE complex assembly. Accordingly, syntaxin-1A confinement was prevented by expression of botulinum neurotoxin type E. The Munc18-1 domain 3a hinge-loop therefore controls syntaxin-1A engagement into SNARE complex formation during priming.

Introduction

The dynamic organization of neurotransmitter receptors on the postsynaptic plasma membrane has emerged as a key regulator of synaptic function (Choquet and Triller, 2013). The reversible trapping by receptor–scaffold interactions is critical to generate nanoscale domains that are deemed essential in mediating both neurotransmission and its plasticity (Nair et al., 2013). Although nanodomains formed by key players that mediate neurotransmitter release have been described (Lang et al., 2001; Zilly et al., 2011; van den Bogaart et al., 2013), surprisingly little is known about the dynamics of transiently trapped molecules in such nanodomains. Our goal was to investigate the precise sequence of inter- and intramolecular events that cause a docked secretory vesicle (SV) to acquire fusion competence, a process called priming. Munc18-1, a key regulator of SV exocytosis, is critically required for SV docking and priming leading to SNARE-dependent hormonal and neurotransmitter release (Verhage et al., 2000; Voets et al., 2001; Toonen et al., 2006). Here, we applied single-molecule imaging (Choquet and Triller, 2013; Kusumi et al., 2014; Trimble and Grinstein, 2015) in an attempt to track the diffusional signature of priming for both Munc18-1 and syntaxin-1A by pinpointing the changes in their spatiotemporal distribution that occurred during stimulation of SV exocytosis.

SV priming requires the presence of a flexible hinge-loop region within Munc18-1 domain 3a (Martin et al., 2013). Here, we demonstrate that removing part of this structure (Munc18-1$^{\Delta317\text{-}333}$) leads to a dramatic increase in the SV docking time at the plasma membrane of PC12 cells deficient in

The Rockefeller University Press $30.00
J. Cell Biol. Vol. 214 No. 7 847–858
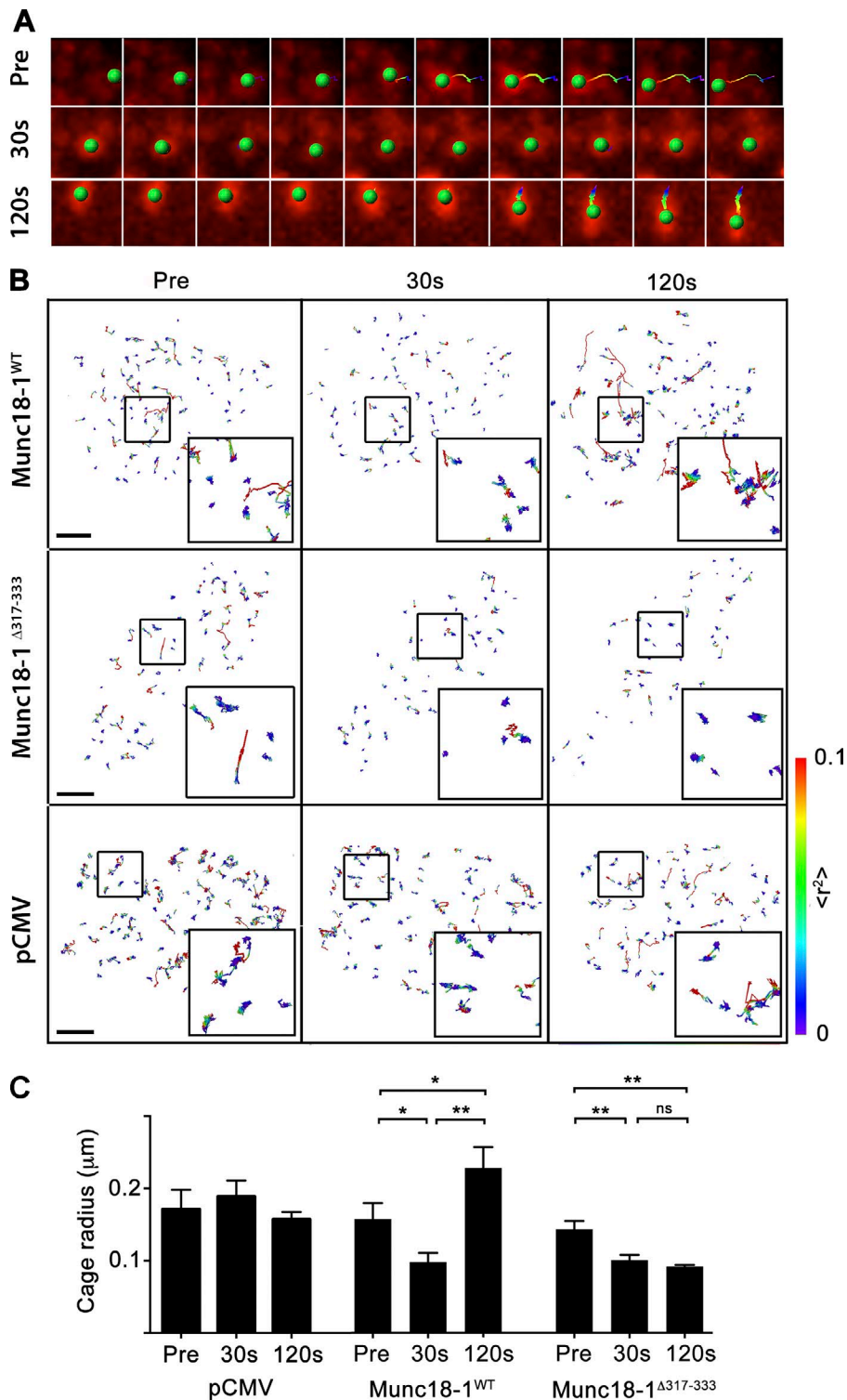www.jcb.org/cgi/doi/10.1083/jcb.201508118

JCB 847

Figure 1. **The duration of SV docking is increased by removing the Munc18-1 domain 3a hinge-loop.** DKD-PC12 cells coexpressing NPY-mCherry and indicated plasmids were imaged by TIRF microscopy at 10 Hz before and during secretagogue stimulation using Ba^{2+} (2 mM). (A) The track of a single SV in DKD-PC12 cells coexpressing NPY-mCherry and Munc18-1^{WT} before and 30 and 120 s after the onset of Ba^{2+} stimulation. Note that the SVs undergo a transient restriction at 30 s, indicative of docking. (B) NPY-mCherry–positive SVs were tracked, and their cage size was analyzed based on their MSD. Track MSD is displayed as indicated in color-coding. Note that the expression of Munc18-1^{WT} rescues transient docking as indicated by the mean cage radius becoming restricted in the first 30 s of stimulation, followed by undocking (top row). In DKD-PC12 cells coexpressing NPY-mCherry and Munc18-1$^{\Delta 317-333}$ (middle row), the mean cage radius of tracked SVs also becomes restricted in the first 30 s of stimulation but remains restricted after 120 s, indicating more stable SV docking. DKD-PC12 cells co-expressing NPY-mCherry and pCMV show no docking phenotype (bottom row). Bars, 5 µm. (C) Quantification of cage sizes before and 30 and 120 s after stimulation. *, $P < 0.05$, **, $P < 0.01$, Student's *t* test. ns, not significant.

endogenous Munc18-1/2 (DKD-PC12 cells). Single-molecule analysis revealed an activity-dependent increase in the mobility of wild-type Munc18-1 (Munc18-1^{WT}) molecules associated with a reduction in nanodomain size, consistent with the release of Munc18-1^{WT} from these domains during priming. Importantly, this effect was abolished upon expression of the Munc18-1$^{\Delta 317-333}$ mutant, suggesting a key role for the hinge-loop in releasing Munc18-1. Our results also revealed that the Munc18-1 and syntaxin-1A nanodomains are closely associated, facilitating a

rapid molecular cross talk that is likely to occur during priming. In contrast to that of Munc18-1, the mobility of syntaxin-1A was significantly reduced during stimulation in DKD-PC12 cells expressing Munc18-1^{WT}, an effect that could be blocked by expressing Munc18-1$^{\Delta 317-333}$ or inhibiting SNARE complex assembly with the botulinum neurotoxin type E light chain (BoNT/E-LC). Munc18-1 therefore promotes syntaxin-1A engagement within the SNARE complex during priming via a "lock-and-go" mechanism triggered by the domain 3a hinge-loop.
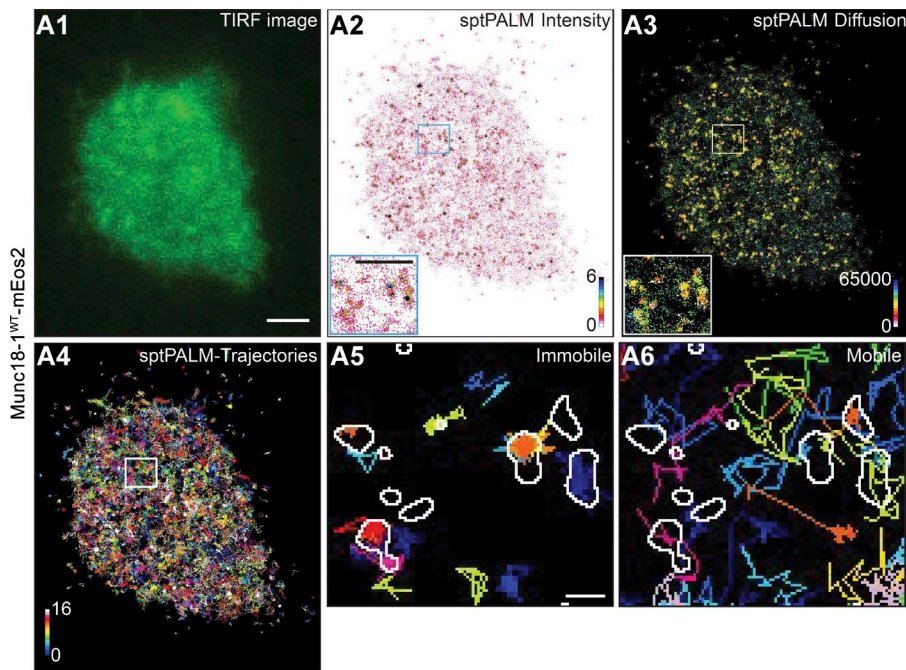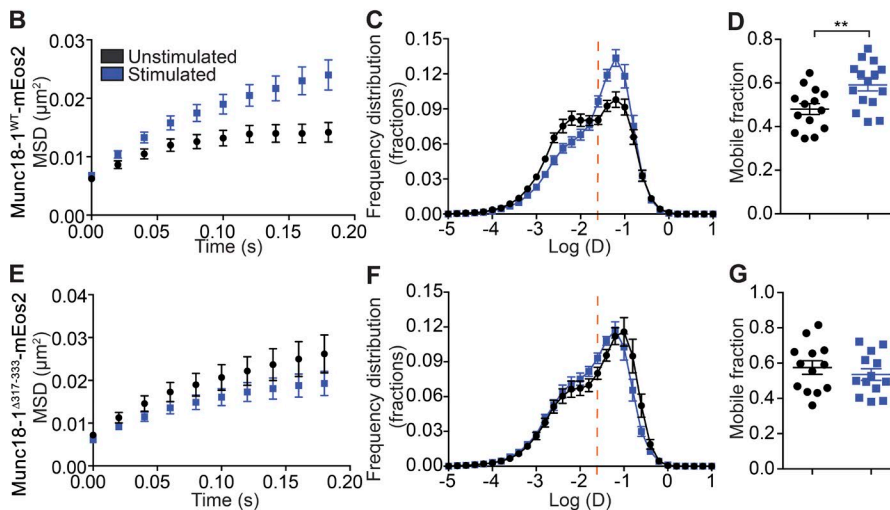
Figure 2. The Munc18-1 3a domain hinge-loop promotes an activity-dependent increase in Munc18-1 mobility. DKD-PC12 cells expressing Munc18-1^{WT}-mEos2 or Munc18-1$^{\Delta317-333}$-mEos2 were imaged at 50 Hz in either unstimulated or stimulated (2 mM Ba^{2+}) conditions. (A) TIRF image (A1), sptPALM mean intensity map (A2), and diffusion coefficient map (A3) of a DKD-PC12 cell (detections range from 10^{-5} to 10^{1} μm^2/s) and trajectory maps. (A4) Trajectory color-coding calculated from 16,000 images (in arbitrary units). (A5 and A6) Nanodomains of Munc18-1 from the mean intensity map (outlined) were overlaid with low-mobility and freely diffusing trajectories. Nanodomains preferentially contain low-mobility molecules. Bars: (A1) 1 μm; (A2, inset) 500 nm; (A5) 100 nm. (B–G) Mean MSD as a function of time and mean distribution of the diffusion coefficient and the mobile fraction in indicated cells and conditions (n = 13–15 cells for each condition). Sidak–Bonferroni adjustments were made while performing multiple *t* test comparisons of mobile fractions (**, P < 0.01). Mean ± SEM.

Results

The Munc18-1 3a domain hinge-loop promotes an activity-dependent increase in Munc18-1 mobility

We, and others, have revealed that a hinge-loop region within Munc18-1 domain 3a plays a key role in SV exocytosis without affecting the role of Munc18-1 in the transport of syntaxin-1A to the plasma membrane (Han et al., 2013; Martin et al., 2013). Because Munc18-1 has previously been shown to control SV docking in neurosecretory cells (Voets et al., 2001; Toonen et al., 2006), we tested whether expression of Munc18-1$^{\Delta317-333}$, a Munc18-1 deletion mutant lacking 17 residues of the domain 3a hinge-loop, could rescue the docking of SVs in DKD-PC12 cells. SVs in DKD-PC12 cells lack the ability to dock at the plasma membrane and to undergo regulated fusion, but fusion can be rescued by reexpressing GFP-Munc18-1 (Martin et al., 2013). Tracking individual SVs containing secretory neuropeptide Y fused to mCherry (NPY-mCherry) in DKD-PC12 cells by total internal reflection fluorescence (TIRF) microscopy before and after secretagogue stimulation did not reveal any notable change in mobility (Fig. 1). In contrast, expression of Munc18-1^{WT} in these cells rescued SV docking, as demonstrated by a significant reduction in SV mobility in the first 30 s of stimulation (Fig. 1, A and B). This effect, which was indicated by a significant decrease in SV confinement area (cage size) calculated from the mean squared displacement (MSD) of individual SV trajectories (Fig. 1 C), was transient, as it was no longer detected 120 s after the onset of stimulation (Fig. 1 C). We noticed that the cage radius at 120 s was significantly larger than that of the prestimulation condition. This could be caused by vesicle replenishment, a process that requires active movement of SVs toward the plasma membrane (Maucort et al., 2014). Importantly, expression of Munc18-1$^{\Delta317-333}$ resulted in a complete rescue of SV docking at 30 s, but remarkably, the undocking of SVs was impaired, as their mobility remained restricted after 120 s. The rescue of a docking phenotype through expression of either Munc18-1^{WT} or Munc18-1$^{\Delta317-333}$ was confirmed by electron microscopy (Fig. S1).

That Munc18-1$^{\Delta 317\text{-}333}$ can rescue vesicle docking but not exocytic fusion events (Martin et al., 2013) suggests that the hinge-loop plays a critical role in priming docked SVs for fusion. To investigate this, we turned to single-molecule imaging of Munc18-1 to measure the changes in mobility patterns associated with SV priming. To generate high-density maps of Munc18-1 localization and mobility at the cell surface, DKD-PC12 cells were transfected with Munc18-1^{WT} fused to photoconvertible mEos2 and imaged by single-particle tracking photoactivated localization microscopy (sptPALM; Manley et al., 2008). We first confirmed that the mEos2 tag did not interfere with the ability of Munc18-1 to rescue neuroexocytosis in DKD-PC12 cells (Fig. S2, A and B). We also checked the expression level of Munc18-1^{WT}-mEos2 in transfected DKD-PC12 cells and found that it was comparable to that of endogenous Munc18-1 in PC12 cells considering a 40–50% transfection efficiency (Fig. S2 C). We then turned to conventional TIRF imaging of Munc18-1^{WT}-mEos2, which produced relatively homogeneous staining with some apparent small puncta (Fig. 2 A1). In contrast, the sptPALM superresolved-intensity image revealed the organization and plasma membrane distribution of Munc18-1^{WT}-mEos2 (Fig. 2, A2 and A3). Tracking individual molecules allowed us to generate maps of their trajectories and instantaneous diffusion coefficients (Nair et al., 2013; Fig. 2 A4), highlighting a high level of heterogeneity in the mobility of Munc18-1^{WT}-mEos2 in unstimulated cells. Indeed, two distinct populations were present, mobile and confined, with the latter representing nanodomains (Fig. 2, A5 and A6). Most punctate structures displayed a relatively restricted radius of diffusion, or "caging," consistent with previous studies of Munc18-1 and syntaxin-1A mobility in resting neurons (Kavanagh et al., 2014; Fig. 2, A5 and A6).

We next analyzed the MSD of the sptPALM trajectories of individual Munc18-1^{WT}-mEos2 molecules to assess changes in mobility in response to Ba^{2+} secretagogue stimulation (Fig. 2, B–G). We compared the MSD of trajectories of Munc18-1^{WT}-mEos2 molecules from unstimulated and stimulated DKD-PC12 cells (Fig. 2 B) and found that the areas under these curves were significantly different (Fig. 3 A). Analysis of the distribution of the diffusion coefficients of Munc18-1^{WT}-mEos2 single-molecule trajectories in unstimulated cells revealed the presence of two distinct populations: an immobile fraction and a mobile fraction (Fig. 2 C; Constals et al., 2015). Importantly, Munc18-1^{WT}-mEos2 mobility was significantly altered in stimulated DKD-PC12 cells, as indicated by changes in the MSD and diffusion coefficient (Fig. 2, B and C). Stimulation resulted in a significant increase in the mobile fraction (Fig. 2 D). This suggests that a population of Munc18-1^{WT}-mEos2 molecules is released from the confinement of nanodomains (Fig. 2, B–D). In comparison to Munc18-1^{WT}-mEos2, the MSD of Munc18-1$^{\Delta 317\text{-}333}$-mEos2 was largely unchanged in the resting cells (Fig. 2 E). Strikingly, we did not detect the same shift toward a more mobile fraction for the hinge-loop deletion mutant after stimulation (Fig. 2, F and G), suggesting that the mutation prevented the activity-dependent release of Munc18-1 from the confinement of nanodomains.

The size of Munc18-1 but not Munc18-1$^{\Delta 317\text{-}333}$ nanodomains is reduced by secretagogue stimulation

Because Munc18-1 is distributed in nanodomains on the plasma membrane (Smyth et al., 2013; Kavanagh et al., 2014), we hypothesized that such an activity-dependent increase in mobility
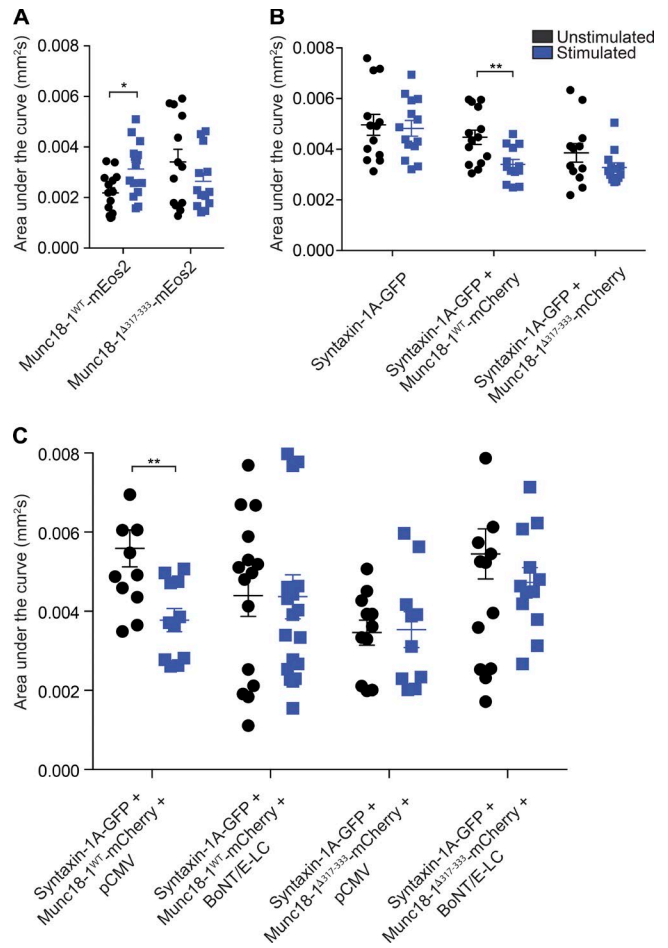
Figure 3. **Area under the MSD curves.** (A–C) DKD-PC12 cells transfected with the indicated plasmids were imaged at 50 Hz (16,000 frames) in either unstimulated or stimulated (2 mM Ba^{2+}) conditions. Area under the MSD curves for each cell in each condition. Sidak–Bonferroni adjustments were made while performing multiple t test comparisons of mobile fractions (*, $P < 0.05$; **, $P < 0.01$). Mean ± SEM.

might lead to a reduction in the number of molecules per nanodomain and a concomitant decrease in their size. To assess this, resting or stimulated DKD-PC12 cells expressing either Munc18-1^{WT}-mEos2 or Munc18-1$^{\Delta 317\text{-}333}$-mEos2 were fixed before PALM imaging (Fig. 4, A–F). To determine the characteristics of the nanodomains of Munc18-1^{WT}-mEos2 and Munc18-1$^{\Delta 317\text{-}333}$-mEos2, an auto-correlation function was applied, which quantifies the spatial distribution of the proteins (Sengupta et al., 2011; Veatch et al., 2012; Harper et al., 2016). Fitting of the values to Eq. 1 enabled us to obtain parameters of the nanodomains. Munc18-1^{WT}-mEos2 molecules exhibited a range of nanodomain sizes (Fig. 4 A), with a radius of 36.0 ± 1.2 nm (mean ± SEM; Fig. 4 C). Importantly, both the mean nanodomain radius and the calculated number of molecules within Munc18-1^{WT}-mEos2 nanodomains were significantly reduced after stimulation (Fig. 4 C). The number of molecules per nanodomain was relatively low (Fig. 4 C), which is likely caused by incomplete conversion of mEos2 (Sengupta et al., 2011). In contrast, the calculated radius and the number of localizations per nanodomain for Munc18-1$^{\Delta 317\text{-}333}$-mEos2 were largely unaffected by stimulation (Fig. 4 F). These results are consistent with a role for the domain 3a hinge-loop in triggering the release of previously immobile Munc18-1 from these nanodomains in response to secretagogue stimulation.
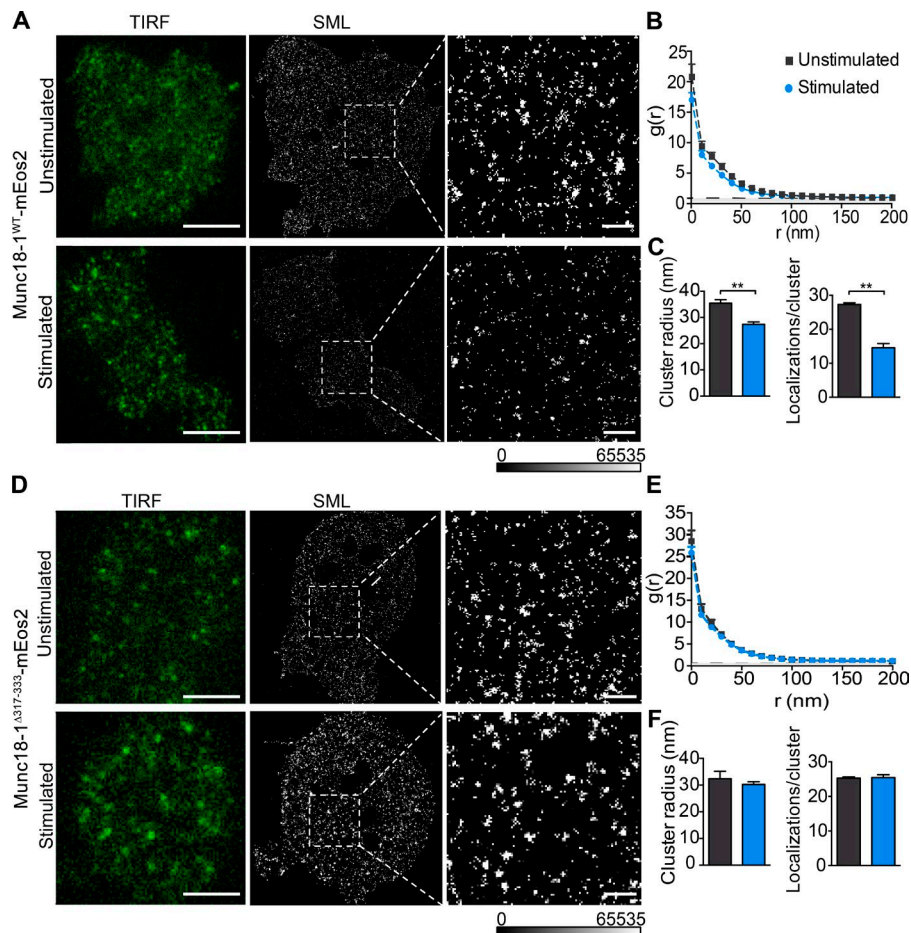
Figure 4. **The size of Munc18-1 but not Munc18-1$^{\Delta317\text{-}333}$ nanodomains is reduced by secretagogue stimulation.** Transfected DKD-PC12 cells expressing Munc18-1^{WT}-mEos2 (A–C) or Munc18-1$^{\Delta317\text{-}333}$-mEos2 (D–F) were incubated with or without 2 mM BaCl$_2$ for 2 min in buffer A, then fixed in paraformaldehyde before single-molecule localization (SML) imaging and processing. (A and D) Representative low-resolution (green fluorescence TIRF) image and corresponding SML image of unstimulated (top) and stimulated (bottom) Munc18-1^{WT}-mEos2 (A) or Munc18-1$^{\Delta317\text{-}333}$-mEos2 (D). Bars: (low-resolution) 2 µm; (enlarged) 200 nm. (B and E) Mean (± SEM) of autocorrelation functions for each region of interest. Three regions of interest were analyzed for each cell, and 10 cells were analyzed for each condition. The experiment was performed three times independently. (C and F) The mean radius (Eq. 1) and the number of molecules per nanodomain (Eq. 2) were obtained from each region of interest by fitting the autocorrelation values. **, P < 0.01, Student's *t* test.

Munc18-1 is critically involved in delivering syntaxin-1A to the plasma membrane (Rickman et al., 2007; Han et al., 2009; Malintan et al., 2009) and in controlling its opening and access to other SNARE proteins (Fasshauer and Margittai, 2004; Rickman et al., 2007; Greitzer-Antes et al., 2013). We therefore investigated whether syntaxin-1A was also present in Munc18-1 nanodomains. DKD-PC12 cells expressing Munc18-1^{WT}-mEos2 or Munc18-1$^{\Delta317\text{-}333}$-mEos2 were fixed and immunolabeled for endogenous syntaxin-1A before dual-color single-molecule imaging. Direct stochastic optical reconstruction microscopy imaging of anti–syntaxin-1A immunolabeling was performed to localize single syntaxin-1A molecules (Heilemann et al., 2008; van de Linde et al., 2011). We found that nanodomains of Munc18-1^{WT}-mEos2 and syntaxin-1A were closely associated, although not fully overlapping (Fig. S3 A). This was particularly prominent in larger nanodomains (Fig. S3 A). Interestingly, expression of Munc18-1$^{\Delta317\text{-}333}$-mEos2 appeared to increase the level of overlap with syntaxin-1A nanodomains (Fig. S3 B). Overall, our results indicate that both syntaxin-1A and Munc18-1 are organized in partially overlapping nanodomains on the plasma membrane, potentially favoring rapid diffusional cross talk.

The Munc18-1 domain 3a hinge-loop controls an activity-dependent decrease in syntaxin-1A mobility

We next examined the effect of Munc18-1 expression on syntaxin-1A mobility in DKD-PC12 cells. We first expressed syntaxin-1A-GFP in these cells. TIRF imaging of syntaxin-1A-GFP revealed a relatively homogeneous staining of the plasma membrane with some apparent small puncta (Fig. 5 A1), similar to the pattern observed for Munc18-1 (Fig. 2 A1). To investigate syntaxin-1A-GFP mobility, we used universal point accumulation imaging in nanoscale topography (uPAINT; Giannone et al., 2010), as the C-terminal GFP tag is exposed to the extracellular space. When a low concentration of ATTO 647N–coupled anti-GFP nanobodies (Kubala et al., 2010) were added to the buffer, stochastic binding of the nanobodies to syntaxin-1A-GFP could be detected during live imaging (Giannone et al., 2010). The uPAINT superresolved intensity images revealed syntaxin-1A nanodomains on the plasma membrane (Fig. 5 A2), as previously described (Lang et al., 2001). Tracking of individual molecules and mapping of their trajectories and instantaneous diffusion coefficients also revealed a high level of heterogeneity (Fig. 5, A3 and A4). Most punctate structures were formed by trajectories exhibiting low diffusion coefficients (Fig. 5 A5). Freely moving molecules were less associated with these nanodomains (Fig. 5 A6). The MSD was calculated for the trajectories of individual syntaxin-1A-GFP molecules to assess potential changes in caging in response to Ba^{2+} stimulation. In DKD-PC12 cells, no significant change was detected in either the MSD or the distribution of diffusion coefficients in response to stimulation (Fig. 5, B and C), as also quantified using the mobile fraction (Fig. 5 D) and area under the MSD curves (Fig. 3 B). Expression of Munc18-1^{WT}-mCherry resulted in a reduced MSD of
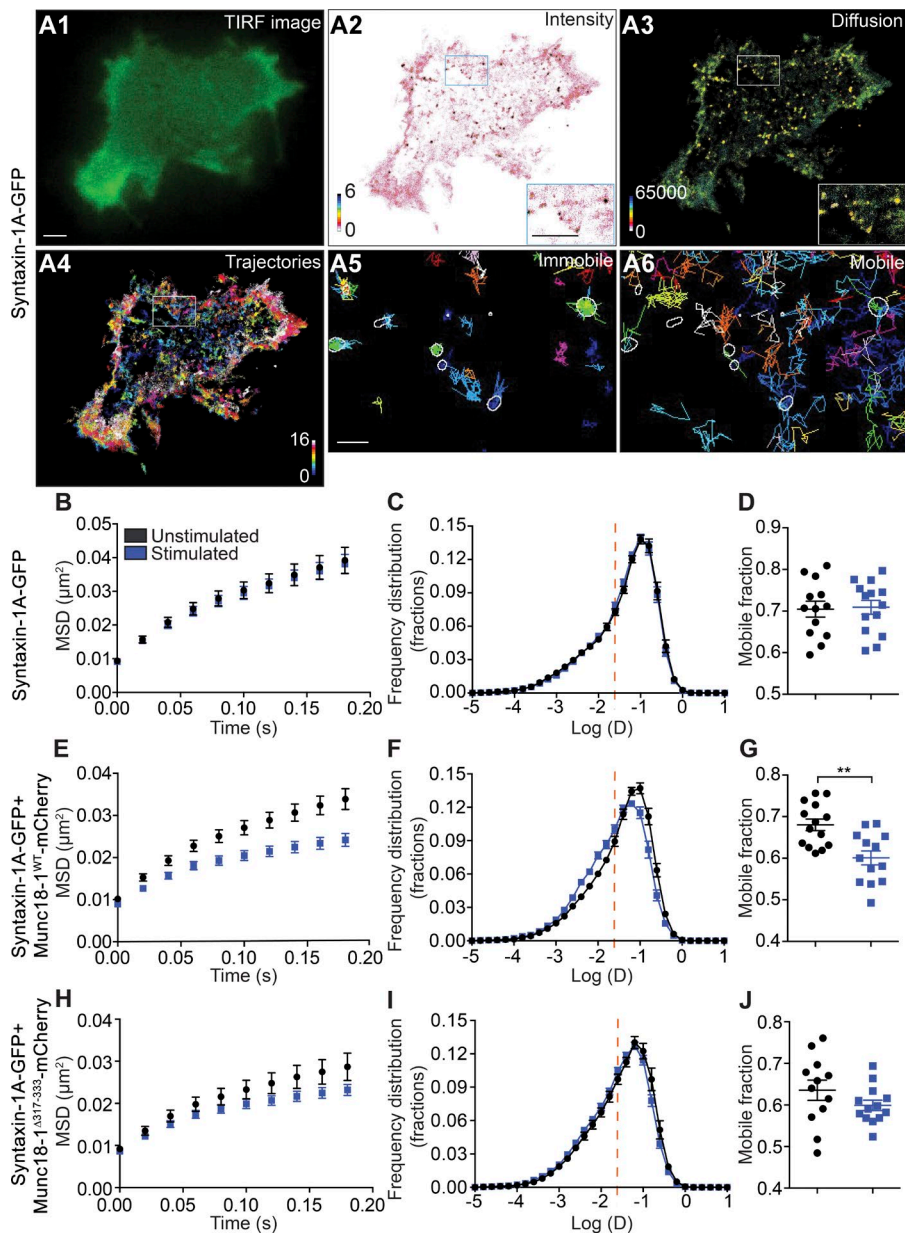
Figure 5. **The Munc18-1 domain 3a hinge-loop controls an activity-dependent decrease in syntaxin-1A mobility.** DKD-PC12 cells expressing syntaxin-1A-GFP alone or with either Munc18-1[WT]-mCherry or Munc18-1[Δ317-333]-mCherry were imaged at 50 Hz (16,000 frames) in either unstimulated or stimulated (2 mM Ba^{2+}) conditions using the uPAINT technique. (A) TIRF image (A1), spt-PALM mean intensity map (A2), and diffusion coefficient map (A3) of a DKD-PC12 cell (detections range from 10^{-5} to 10^1 µm²/s) and trajectory maps (A4) calculated from 16,000 images (trajectory color-coding in arbitrary units). (A5 and A6) Nanodomains of syntaxin-1A-GFP from the mean intensity map (outlined) were overlaid with low-mobility and freely diffusing trajectories. Nanodomains preferentially contain low-mobility molecules. Bars: 1 µm; (insets) 22 nm. (B–J) Mean MSD as a function of time, mean distribution of the diffusion coefficients, and the mobile fraction in indicated cells and conditions (n = 12–14 cells for each condition). Sidak–Bonferroni adjustments were made while performing multiple t test comparisons of mobile fractions (**, $P < 0.01$). Mean ± SEM.

syntaxin-1A-GFP diffusion in unstimulated cells (Fig. 5, E–G). Moreover, the MSD of syntaxin-1A-GFP was significantly reduced in response to Ba^{2+} stimulation, demonstrating that the cage size of syntaxin-1A was also reduced during activity (Figs. 3 B and 5 E). Importantly, the distribution of the diffusion coefficients was also altered by stimulation, leading to a concomitant increase in the immobile fraction and a decrease in the mobile fraction (Fig. 5, F and G). We previously demonstrated that the expression of Munc18-1[Δ317-333] is able to fully rescue syntaxin-1A transport to the plasma membrane in DKD-PC12 cells (Martin et al., 2013). We therefore asked whether this mutant could also control the activity-dependent change in syntaxin-1A mobility. Although we observed a slight reduction in mobility, this was not significantly different from the unstimulated condition, suggesting that the hinge-loop deletion mutant lacks the ability to control syntaxin-1A mobility (Fig. 3 B and Fig. 5, H–J). These results were confirmed by sptPALM of syntaxin-1A-mEos2 cotransfected with untagged Munc18-1[WT] or Munc18-1[Δ317-333] (Fig. S4).

BoNT/E-LC expression prevents the activity-dependent decrease in syntaxin-1A mobility

We predicted that the reduced mobility of syntaxin-1A elicited by activity might stem from its incorporation into the trans-SNARE complex with SNAP-25. To test this hypothesis, we used BoNT/E-LC. BoNT/E-LC enzymatic activity targets SNAP-25 and cleaves 26 residues from the C-terminus of the molecule, thereby blocking neuroexocytosis (Schiavo et al., 1993). The light chains prevent SNARE complex formation (Hayashi et al., 1994), and BoNT/E has an additional effect on the syntaxin-1A/SNAP-25 heterodimer (Rickman et al., 2004). BoNT/E-LC was cotransfected with syntaxin-1A-GFP in DKD-PC12 cells. Our results revealed that the activity-dependent decrease in syntaxin-1A-GFP mobility (Fig. 6, A–C) was blocked by coexpression of Munc18-1[WT]-mCherry and BoNT/E-LC (Fig. 3 C and Fig. 6, D–F). This strongly suggests that the reduction in syntaxin-1A mobility results from syntaxin-1A engagement in the SNARE complex. A similar result was obtained in PC12 cells containing endogenous Munc18-1 (Fig. S5), further high-
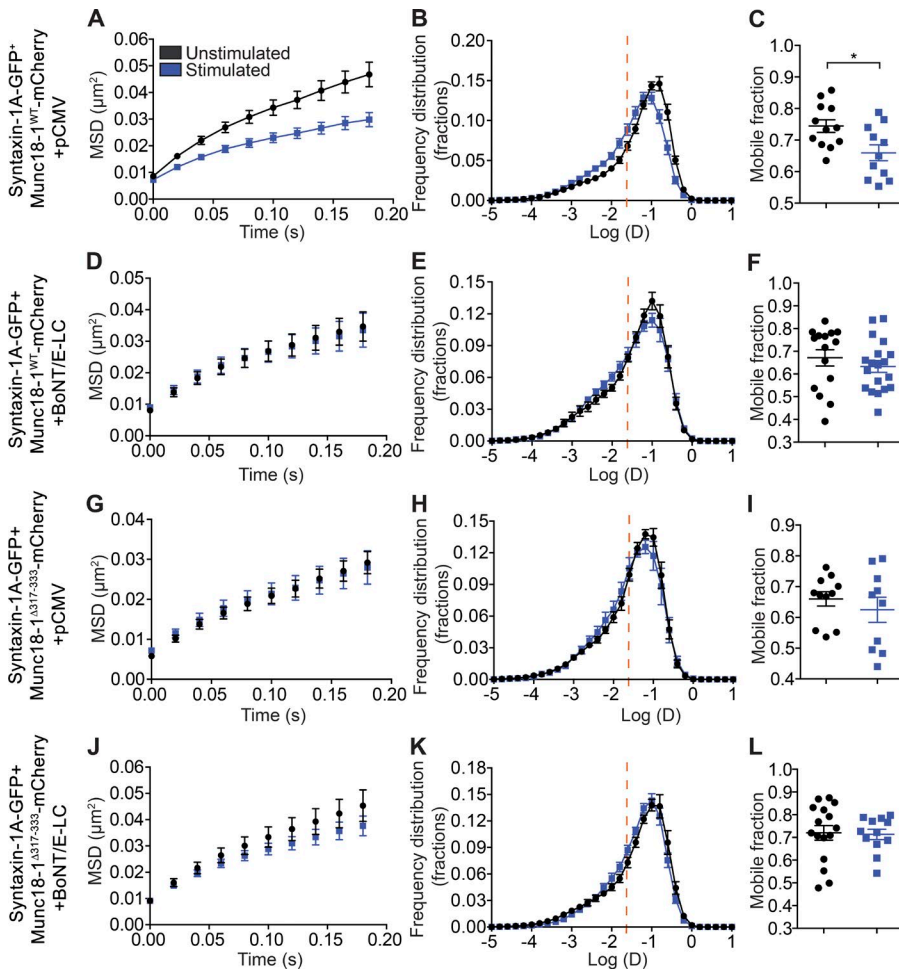
Figure 6. **BoNT/E-LC expression prevents the activity-dependent decrease in syntaxin-1A mobility.** (A–L) DKD-PC12 cells transfected with the indicated plasmids were imaged at 50 Hz (16,000 frames) in either unstimulated or stimulated (2 mM Ba^{2+}) conditions using the uPAINT technique. Mean MSD as a function of time, mean distribution of the diffusion coefficients, and ratio of mobile versus immobile fraction in indicated cells and conditions. (n = 10–19 cells for each condition). Sidak–Bonferroni adjustments were made while performing multiple t test comparisons of mobile fractions (*, P < 0.05). Mean ± SEM.

lighting the importance of Munc18-1 in mediating this effect. To assess whether the domain 3a hinge-loop was responsible for the activity-dependent reduction in syntaxin-1A-GFP mobility, we expressed Munc18-1$^{\Delta 317\text{-}333}$-mCherry either alone (pCMV) or in conjunction with BoNT/E-LC in DKD-PC12 cells and found that both conditions equally inhibited this confining effect and that no additive change was detected upon coexpression of Munc18-1$^{\Delta 317\text{-}333}$-mCherry and BoNT/E-LC (Fig. 6, G–L).

Discussion

Our study demonstrates that the Munc18-1 domain 3a hinge-loop controls a key step in vesicular priming involving syntaxin-1A engagement into the trans-SNARE complex. We first demonstrated that rescuing the expression of Munc18-1$^{\Delta 317\text{-}333}$ leads to both a block of exocytosis (Han et al., 2013; Martin et al., 2013) and a prolonged docking phenotype, suggesting that the Munc18-1 domain 3a hinge-loop plays a role in priming docked vesicles.

Single-molecule analysis allowed us to demonstrate that Munc18-1 becomes more mobile during the course of exocytosis, leading to a reduction of the size and number of molecules present in Munc18-1 nanodomains. The release of Munc18-1 from nanodomains also depended on the domain 3a hinge-loop, as it was not observed with Munc18-1$^{\Delta 317\text{-}333}$. The observed dynamic change in the nanoscale organization of the Munc18-1 clusters is likely to be caused by a conformational switch that

occurred in the domain 3a hinge-loop, as previously hypothesized (Hu et al., 2011). Syntaxin-1A mobility was decreased during stimulation, an effect that was abrogated by the expression of Munc18-1$^{\Delta 317\text{-}333}$, which we further demonstrated resulted from SNARE complex assembly. This effect was also abrogated by expression of Munc18-1$^{\Delta 317\text{-}333}$. Importantly, we cannot rule out that some of the changes detected in the mobility could stem from the incorporation of vesicular proteins on the plasma membrane as a result of exocytosis or a change in plasma membrane fluidity or both.

Munc18-1 interacts with syntaxin-1A in its closed conformation, inhibiting its interaction with other SNARE proteins (Misura et al., 2000). Our results therefore suggest that a conformational change in the Munc18-1 domain 3a hinge-loop leads to the opening of syntaxin-1A that allows SNARE complex formation and a relative immobilization of syntaxin-1A molecules. Indeed, blocking SNARE assembly with BoNT/E-LC also prevented the reduction in syntaxin-1A mobility. An important aspect of our study was the discovery of the dissociation of Munc18-1, presumably from syntaxin-1A during or after SNARE complex assembly.

The Munc18-1 domain 3a hinge-loop therefore acts as a dual trigger that promotes both syntaxin-1A incorporation into the trans-SNARE complex and the concomitant release of Munc18-1 (Fig. 7). The opening of syntaxin-1A and the disassembly of Munc18-1 (Gerber et al., 2008) are therefore likely to enable its subsequent interaction with SNAP25. It has been proposed that the Munc18-1 hinge-loop can undergo a significant
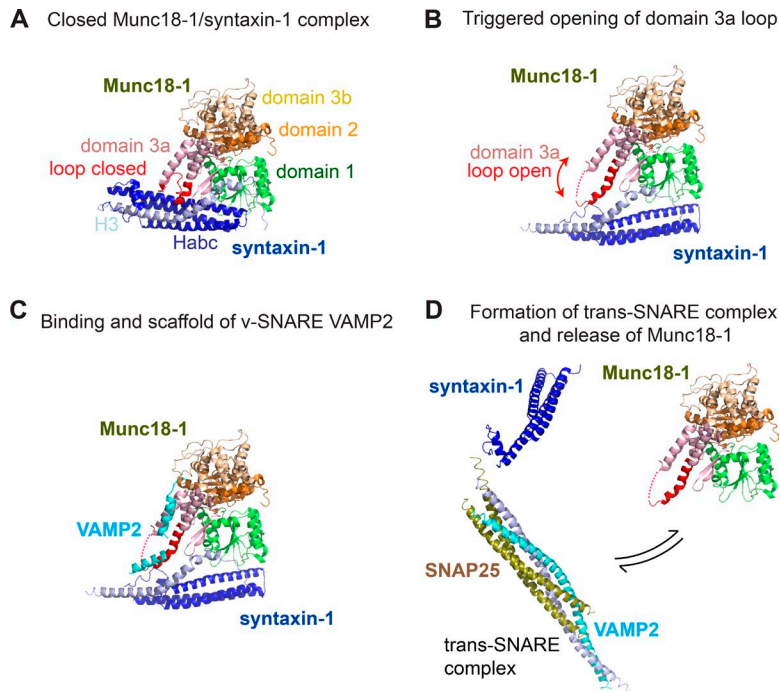
A Closed Munc18-1/syntaxin-1 complex

B Triggered opening of domain 3a loop

C Binding and scaffold of v-SNARE VAMP2

D Formation of trans-SNARE complex and release of Munc18-1

Figure 7. **Schematic of the fate of the Munc18-1.** (A) Syntaxin-1A interacts with Munc18-1 in a closed conformation during trafficking and before stimulation of exocytosis. (B) A conformational change in the Munc18-1 domain 3a loop (triggered by unknown mechanisms) leads to the opening of syntaxin-1A. The closed conformation in the first panel has been observed in a crystal structure of a complex of Munc18-1 and the soluble portion of syntaxin-1A (Burkhardt et al., 2008). The extended conformation of Munc18-1 domain 3a depicted here is observed in Sec1/Munc18 proteins crystallized in the absence of SNARE partners (Hu et al., 2011). (C and D) The domain 3a loop provides a platform for interacting with the v-SNARE VAMP2, allowing assembly of syntaxin-1A with VAMP2 and SNAP-25. This model is based on the structure of the yeast SM protein Vps33 and the cognate v-SNARE Nyv1 reported by Baker et al. (2015).

conformational change, adopting an extended structure that precludes binding to "closed" syntaxin-1A (Hu et al., 2011; Fig. 7, A and B). The extended hinge-loop has also been suggested to bind directly to VAMP2 and promote SNARE assembly and vesicle fusion (Fig. 7, C and D; Parisotto et al., 2014). Our data showing the opposing changes in Munc18-1 and syntaxin-1A mobility suggest that Munc18-1 engages syntaxin-1A into the trans-SNARE complex before being disassembled during priming, which is suggestive of a lock-and-go mechanism. Although our data suggest that Munc18-1 is released from syntaxin-1A, it is still unclear whether this release occurs before or after syntaxin-1A engagement into the SNARE complex. The latter hypothesis would imply that Munc18-1 undergoes a transient reduction in mobility during syntaxin-1A engagement before its release. We did not detect such a transient confinement in our experiments, suggesting this is not the case, although this could possibly be caused by the limited temporal resolution of our data acquisition. Alternatively, Munc18-1 release could occur before syntaxin-1A engagement and simply control the level of opened syntaxin-1A available in nanodomains of the plasma membrane. Future experiments will be key to distinguishing between these two possibilities.

Materials and methods

Plasmids

Syntaxin-1A-GFP was generated from pECFP-N1 syntaxin-1A provided by Y. Liu (University of Oklahoma, Norman, OK). In brief, syntaxin-1A was double-digested with XhoI and SmaI and subcloned into pEGFP-N1 using T4 DNA ligase (New England Biolabs, Inc.). Syntaxin-1A-mEos2 was generated from pECFP-N1 syntaxin-1A. In brief, PCR was used to amplify mEos2 from pRSETa-mEos2 obtained from C. Mulle (University of Bordeaux, Bordeaux, France) using the following primers: forward, 5′-GATCCACCGGTCGCCACCATGAGT GCGATTAAGCCAGA-3′; reverse, 5′-CTTGTACAGCTCTTATCG TCTGGCATT-3′. It was then subcloned into pECFP-N1 syntaxin-1A

using AgeI and BsRGI, replacing ECFP. pmEos2-N1 was generated from pRSETa-mEos2 (provided by C. Mulle) and pEGFP-N1 (Takara Bio Inc.). mEos2 was amplified by PCR using the following primers: forward, 5′-GATCCACCGGTCGCCACCATGAGTGCGATTAAG CCAGA-3′; reverse, 5′-CTTGTACAGCTCTTATCGTCTGGCATT-3′. It was then subcloned into pEGFP-C1 using AgeI and BsRGI, to replace EGFP. Munc18-1^{WT}-mEos2 and Munc18-1$^{\Delta317-333}$-mEos2 were generated from pCMV-Munc18-1^{WT}-emGFP and the $\Delta317$-333 mutant (Martin et al., 2013). Munc18-1 was amplified by PCR using the following primers: forward, 5′-CGTCAGATCCGCTAGCGGCCA CCATGGCCCCCATT-3′; reverse, 5′-GTCGACTGCAGAATTCGA AGACTGCTTATTTCTTCGTCT-3′. It was then subcloned into the pmEos2-N1 multiple cloning site at NheI and EcoRI using the InFusion system (Takara Bio Inc.). All constructs were sequenced in the Australian Genome Research Facility at the University of Queensland, Brisbane, QLD, Australia. Munc18-1^{WT}-mCherry and Munc18-1$^{\Delta317-333}$-mCherry were made by PCR amplification of Munc18-1 using the forward primer (5′-CGTCAGATCCGCTAGCGGCCACCATGGCCC CCATT-3′) and reverse primer (5′-GTCGACTGCAGAATTCGAAGA CTGCTTATTTCTTCGTCT-3′) from pCMV-Munc18-1-EmGFP and were inserted into pmCherry-N1 between the NheI and EcoRI sites by InFusion (as per the manufacturer's instructions). BoNT/E-LC was a gift from T. Binz (Hannover Medical School, Hannover, Germany; Vaidyanathan et al., 1999). BoNT/E-LC was cloned with a far-red fluorescent protein by BioWit.

pCMV-neuropeptide Y-mCherry (NPY-mCherry) has been described previously (Papadopulos et al., 2015). Untagged Munc18-1^{WT} and Munc18-1$^{\Delta317-333}$ used for cotransfection with syntaxin-1A-GFP in DKD-PC12 cells have been described (Martin et al., 2013). pCMV-NPY-hPLAP was provided by S. Sugita (University of Toronto and University Health Network, Toronto, ON, Canada).

Cell cultures and transfections

DKD-PC12 cells were maintained as described previously (Han et al., 2009), supplemented with 2.5 µg/ml plasmocin (ant-mpt; InvivoGen). For single-molecule experiments, cells were transfected with Munc18-1-mEos2 or Munc18-1$^{\Delta317-333}$-mEos2. For uPAINT experiments, cells

were cotransfected with syntaxin-1A-GFP alone or with either Munc18-1-mCherry or Munc18-1$^{\Delta317\text{-}333}$-mCherry. Triple-transfection uPAINT experiments were also performed. DKD-PC12 cells were transfected with the following combinations: (a) syntaxin-1A-GFP, Munc18-1-mCherry, and pCMV; (b) syntaxin-1A-GFP, Munc18-1-mCherry, and BoNT/E-LC; (c) syntaxin-1A, Munc18-1$^{\Delta317\text{-}333}$-mCherry, and pCMV; and (d) syntaxin-1A-GFP, Munc18-1$^{\Delta317\text{-}333}$-mCherry, and BoNT/E-LC. Cells were left for 24 h in their respective dishes and then plated on poly-D-lysine–coated glass-bottom culture dishes (MatTek Corporation). Imaging was performed 72 h after transfection. Pheochromocytoma (PC12) cells were maintained at 37°C, 5% CO_2 in DMEM supplemented with 5% Serum Supreme (Lonza), 5% heat-inactivated horse serum (Gibco), and 0.5% GlutaMAX (Gibco). Cells were transfected with syntaxin-1A-mEos2 or cotransfected with TagRFP657-BoNT/E-LC using Lipofectamine LTX reagent according to the manufacturer's instructions. After 48 h, cells were plated on poly-D-lysine–coated glass-bottom culture dishes (MatTek Corporation) and processed for live cell imaging.

Antibodies

Rabbit anti-SNAP25E (1:1,000) was obtained from D. Sesardic (National Institute for Biological Standards and Control, South Mimms, England, UK). Mouse anti–β-actin clone AC-74 (1:20,000) and mouse anti–syntaxin-1A (1:1,000) were purchased from Sigma-Aldrich. Anti-mouse (IRDye 680 or 800) and anti-rabbit (IRDye 680 or 800) infrared antibodies were used for Western blotting (1:25,000; LI-COR Biosciences). The anti–mouse IgG secondary antibody labeled with Alexa Fluor 647 (1:500) was obtained from Invitrogen.

Correlative light and electron microscopy

DKD-PC12 cells expressing pCMV, Munc18-1$^{\text{WT}}$-emGFP, and Munc18-1$^{\Delta317\text{-}333}$-emGFP were seeded on gridded poly-D-lysine–coated glass-bottom culture dishes. After 24 h, cells were fixed in 2.5% glutaraldehyde in PBS. Bright-field and epifluorescence images were taken using a 10× air objective on a microscope (Axio Imager; ZEISS). The coordinates of transfected cells were noted, and the cells were then processed for transmission correlative light and electron microscopy. Specifically, the fixed cells were contrasted with 1% osmium tetroxide and 4% uranyl acetate before dehydration and embedding in LX-112 resin.

Sections (∼50 nm) were cut using an ultramicrotome (UC64; Leica Biosystems) and imaged using a transmission electron microscope (model 1011; JEOL) equipped with a cooled charge-coupled device camera (Morada; Olympus). All images were processed using Photoshop CS3 (Adobe Systems), and figures were compiled with Illustrator CS3 (Adobe Systems).

Single-vesicle trajectories

DKD-PC12 cells were cotransfected with NPY-mCherry and pCMV, untagged Munc18-1$^{\text{WT}}$, or Munc18-1$^{\Delta317\text{-}333}$ and seeded on glass-bottom culture dishes. Cells were bathed in buffer A (145 mM NaCl, 5 mM KCl, 1.2 mM Na_2HPO_4, 10 mM D-glucose, and 20 mM Hepes, pH 7.4). Time-lapse videos were captured by TIRF microscopy at 10 frames/s at 37°C. Cells were imaged for 3 min before and after the addition of 2 mM $BaCl_2$.

Particle tracking of NPY-mCherry–labeled SVs was performed as described previously (Papadopulos et al., 2015). Using the spot-tracking function of Imaris (Version 7.3.1; Bitplane AG), SVs were tracked in previously acquired TIRF images before and after Ba^{2+} stimulation during the indicated time periods. The spot diameter was 0.30 μm, and vesicles were selected based on local contrast thresholding after background subtraction. Tracking was performed using the built-in autoregressive motion model with maximum displacement of 0.5 μm per

time step and a gap size of 1 frame. The MSD was calculated for each vesicle over incrementing time intervals and then averaged.

To characterize vesicle mobility, MSD data were fitted to a confined diffusion model (Saxton, 1993). In this model, the MSD is described as follows and provides a second-order approximation of vesicle diffusion within a finite space or cage:

$$MSD(\Delta t) \ = \ r_c^2 \Big[1 - A_1 \exp \Big(-\frac{4A_2 D}{r_c^2} \Delta t \Big) \Big],$$

Where A_1 and A_2 are constants determined by the cage geometry, with $A_1 = 0.99$ and $A_2 = 0.85$ for circular cages (Saxton, 1993; Saxton and Jacobson, 1997); D is the diffusion coefficient of a particle within the cage; and r is the radius of the circular cage in which an infinitesimally small particle is free to diffuse with diffusion coefficient D_α. Only SVs tracked for >40 consecutive frames were considered.

Live imaging

TIRF microscopy. For live-cell TIRF microscopy, transfected cells were visualized on a TIRF microscope (Roper Technologies) equipped with an ILas^2 double laser illuminator (Roper Technologies), a CFI Apo TIRF 100× (1.49-NA) objective (Nikon), and an Evolve512 delta EMCCD camera (Photometrics). Image acquisition was performed using Metamorph software (version 7.7.8; Molecular Devices). Cells were bathed in buffer A.

sptPALM. Time-lapse TIRF movies were captured at 50 Hz (16,000 frames) at 37°C for both control and stimulated cells. $BaCl_2$ (2 mM) was added immediately before initiating image acquisition to stimulate the cells. For PALM, a 405-nm laser was used to photoactivate the cells expressing mEos2-tagged constructs, and a 561-nm laser was simultaneously used for excitation of the resulting photoconverted molecules. To isolate the mEos2 signal from autofluorescence and background signals, we used a double-beam splitter (LF488/561-A-000; Semrock) and a double-band emitter (FF01-523/610-25; Semrock). To spatially distinguish and temporally separate the stochastically activated molecules during acquisition, the power of the lasers was adjusted such that the 405-nm laser used 5–6% of initial laser power (100 mW; Vortran Laser Technology) and the 561-nm laser used 75–80% of initial laser power (150 mW; Cobolt Jive).

uPAINT. uPAINT experiments were performed as per Giannone et al. (2010). To track syntaxin-1A-GFP, we used a GFP nanobody (Kubala et al., 2010) conjugated to ATTO 647N-NHS-ester (Atto-Tec). DKD-PC12 cells were transfected with syntaxin-1A-GFP alone or cotransfected with either Munc18-1-mCherry or Munc18-1$^{\Delta317\text{-}333}$-mCherry. ATTO 647N–coupled anti-GFP nanobodies were added at a low concentration for stochastic labeling. Time-lapse TIRF videos were captured at 50 Hz (16,000 frames by image streaming) at 37°C. Separate cells were imaged in control conditions or stimulated (imaging was initiated upon addition of 2 mM $BaCl_2$). We used a quadruple beam splitter (LF 405/488/561/635-A-000-ZHE; Semrock) and a quad band emitter (FF01-446/510/581/703-25; Semrock). The power of the 635-nm laser used was 75–80% of initial laser power (200 mW).

sptPALM analysis. The localization and dynamics of single molecules were acquired from the extracted 16,000 TIRF images as previously described (Nair et al., 2013). In brief, the combination of wavelet segmentation (Izeddin et al., 2012) and simulated annealing was used to detect and track each molecule. PALM-Tracer, a custom-written program that runs as a plug-in in Metamorph software (Molecular Devices), was used to localize the molecules and quantify the dynamics of the proteins. The diffusion coefficient (D) distribution was sorted into two groups. The first group, composed of molecules with a D value <0.0312 μm²/s, was referred to as immobile. The $D_{\text{threshold}} = 0.0312$ μm²/s was calculated as previously

described (Constals et al., 2015). The second group was defined as the mobile fraction and composed of molecules with D values higher than 0.0312 µm²/s. The color-coding for the superresolved images was performed using ImageJ. The color-coding of the trajectory maps are arbitrary units of 16 colors. The color gradient represents the time of the detection of the tracks in the video. Blue trajectories indicate detection early in the video, whereas pink indicates the late trajectories. In the average-intensity maps, each pixel indicates an individual molecule. The area with the highest density is represented in black, whereas white represents regions with no detection. The color-coding of the diffusion maps ranges from 15,000 units to 50,000, corresponding to diffusion coefficients of 10^{-5} and 10 µm²/s, respectively.

NPY-hPLAP release assay

DKD-PC12 cells were transfected with NPY fused to the catalytic domain of human placental alkaline phosphatase (NPY-hPLAP) and pCMV vector, pCMV-Munc18-1^{WT}-emGFP, or Munc18-1^{WT}-mEos2 for 48 h. Cells were washed and incubated with PSS buffer as a control (145 mM NaCl, 5.6 mM KCl, 0.5 mM MgCl$_2$, 5.6 mM glucose, and 15 mM Hepes-NaOH, pH 7.4) or stimulated with high K$^+$-PSS buffer (81 mM NaCl, 70 mM KCl, 2.2 mM CaCl$_2$, 0.5 mM MgCl$_2$, 5.6 mM glucose, and 15 mM Hepes-NaOH, pH 7.4) for 15 min at 37°C. NPY-hPLAP released from cells was measured using the chemiluminescent reporter gene assay system (Phospha-Light; Applied Biosystems) according to the manufacturer's instructions, and the results were expressed as a percentage of control (low K$^+$).

Western blotting

PC12 and DKD-PC12 cells, either untransfected or expressing Munc18-1^{WT}-mEos2 (as per figure legends), were harvested 48–72 h after transfection into 2× Laemmli sample buffer containing 25 mM DTT, passed through a 25-gauge needle, boiled for 5 min at 95°C, and run on 10–12% SDS-PAGE gels, after which Western blotting was conducted with antibodies as indicated (rabbit anti-VAMP2, #104 202; Synaptic Systems; mouse anti–β-actin [AC15], #ab6276; Abcam; mouse anti–Munc18-1, #610336; BD).

Single-molecule localization microscopy and data analysis

Transfected DKD-PC12 cells expressing Munc18-1-mEos2 or Munc18-1$^{\Delta317\text{-}333}$-mEos2 were incubated in buffer A alone or stimulated with 2 mM Ba^{2+} for 2 min. The cells were then fixed with 4% paraformaldehyde diluted in PBS for 45 min and washed in PBS. Tetraspeck beads (0.1 µm; Invitrogen) were added before the acquisition of images on an ELYRA PS1 microscope (ZEISS) equipped with a 100× objective (alpha Plan-Apochromat 100×/1.46 oil-immersion) and an EMCCD camera. mEos2 molecules were simultaneously photoconverted with a 405-nm laser and excited using a 561-nm laser, as described earlier. For each dataset, 20,000 frames were acquired at a rate of 33 Hz, at which point the majority of mEos2-tagged molecules had been photoconverted.

The acquired time-lapse videos were processed to retrieve the coordinates of individual localizations using Zen software (ZEISS). The datasets were corrected for x,y drift using the fluorescent Tetraspeck beads as fiducial markers, and fluorescent molecules imaged in multiple frames were compensated for by consolidating those that appeared within 1 frame and 1 pixel of one. Datasets were further filtered by excluding all points with a localization precision <10 nm or >40 nm. To examine the superresolved distribution of Munc18-1 on the plasma membrane, single-molecule localization images were reconstructed from the filtered coordinates with a pixel size of 10 nm and were used for further analysis.

A custom-written program in Matlab (Mathworks) was used to quantify the spatial distribution and degree of clustering of Munc18 molecules through the use of an autocorrelation function (Harper et al., 2016). This method of analysis uses fast Fourier transforms to quantify the spatial distribution of molecules by providing information on the likelihood of finding a molecule at a given distance from another molecule (Sengupta et al., 2011; Veatch et al., 2012). The analysis was applied to regions of interest selected from reconstructed images. The calculated autocorrelation [$g(r)$] values were fitted to the following equation to obtain the characteristics of the nanodomains:

$$g(r) = \left(\frac{1}{2\pi\sigma^2\rho}\right)\exp\left(\frac{-r^2}{2\sigma^2}\right) + A\exp\left(\frac{-r^2}{\xi}\right) + C, \quad (1)$$

where ρ is the density of the image, σ is the standard deviation of the point spread function, and A is the amplitude of the exponential decay function. The mean radius of the nanodomains was determined by ξ, which is also known as the correlation length. From these values, the mean number of molecules per nanodomain could be estimated (Sengupta et al., 2011):

$$N_{Cl} \approx 2\pi A\xi\rho_{av}. \quad (2)$$

Dual-color single-molecule localization microscopy

DKD-PC12 cells transfected with Munc18-1-mEos2 or Munc18-1$^{\Delta317\text{-}333}$-mEos2 were fixed as described earlier and processed for immunocytochemistry. Cells were blocked and permeabilized with blocking buffer (2% [wt/vol] BSA, 0.1% [vol/vol] fishskin gelatin, and 0.1% [wt/vol] saponin in PBS) before incubation with the primary antibody (anti–syntaxin-1A) diluted in blocking buffer. The cells were washed with PBS and added to the secondary antibody (Alexa Fluor 647; Dempsey et al., 2011) diluted in blocking buffer. They were then washed in PBS, and Tetraspeck beads were added before imaging. Imaging was performed in a reducing buffer with oxygen scavengers (Nair et al., 2013) to enable photoconversion of Alexa Fluor 647 (Heilemann et al., 2008; van de Linde et al., 2011) on an ELYRA PS1 microscope (ZEISS) equipped with a 100× objective (alpha Plan-Apochromat 100×/1.46 oil-immersion) and an electron-multiplying charge-coupled device camera. The two channels were imaged sequentially, with Alexa Fluor 647 acquired before the mEos2 images.

The resulting time-lapse videos were processed using Zen software as described earlier. In brief, the images were processed to retrieve coordinates, the x,y drift was corrected, the localizations were consolidated, and the two channels were spatially aligned using the fiducial beads in the image. The images were reconstructed with a pixel size of 10 nm.

Marianas TIRF microscopy

After transfection, PC12-DKD cells were visualized with a TIRF microscope (Marianas Everest; Intelligent Imaging Innovations, Inc.) fitted with a 100× oil immersion objective (NA 1.46; ZEISS). Images were acquired using an electron-multiplying charge-coupled device camera (QuantEM 512SC; Photometrics) and SlideBook software (version 5.5.2 × 64; Intelligent Imaging Innovations, Inc.) for the acquisition of images. Cells were bathed in Buffer A (145 mM NaCl, 5 mM KCl, 1.2 mM Na$_2$HPO$_4$, 10 mM D-glucose, and 20 mM Hepes, pH 7.4) before the addition of 2 mM Ba^{2+}, and a time-lapse simultaneous acquisition was captured at 20 Hz for the indicated period. Green mEos2 Alexa Fluor 488 fluorescence was detected using the 488-nm laser line. mEos2 was photoconverted through illumination with a 405-nm laser, and converted molecules were observed with excitation at 561 nm. The syntaxin-1A-mEos2 molecules were tracked for 10 min before stimulation with Ba^{2+}, then tracked for another 5 min. Particle tracking

of syntaxin-1A-mEos2 was performed on previously acquired TIRF images using the Palm Tracer and Metamorph software as previously explained in sptPALM analysis.

Statistics

For the single-particle tracking experiments, each cell was analyzed independently, and the distribution of the diffusion coefficients was computed from 5,000–12,000 trajectories. Median values for the MSD of each analyzed cell were calculated from 5,000–12,000 trajectories. The mean value of the median was plotted against time and shown in the figures. The mobile fraction from the diffusion coefficient distribution for each individual cell was plotted to illustrate cell-to-cell variability. In addition, the area under each MSD curve was calculated for statistical testing. Sidak–Bonferroni adjustments were made while performing multiple t test comparisons of mobile fractions and area under the MSD curves in Prism 6. Values are expressed as mean ± SEM. Post hoc power was computed using the power calculator mentioned in Faul et al. (2009), with $\alpha = 5\%$. The mean power value estimated was 0.86 (range, 0.71–0.94; Faul et al., 2009).

Online supplemental material

Fig. S1 shows the role of Munc18-1 and Munc18-1$^{\Delta317\text{-}333}$ in rescuing the docking of SVs in DKD-PC12 cells. Fig. S2 shows the release assay from DKD-PC12 expressing Munc18-1^{WT} tagged with mEos2 or GFP and comparison of the expression levels of mEos2-tagged Munc18-1^{WT} in DKD-PC12 to endogenous Munc18-1 in PC12 cells. Fig. S3 shows the association of Munc18-1 or Munc18-1$^{\Delta317\text{-}333}$ nanodomains with syntaxin-1A nanodomains. Fig. S4 shows the experiments performed using Marianas TIRF microscopy illustrating the role of Munc18-1 domain 3a hinge-loop in controlling the mobility of syntaxin-1A tagged with mEos2 in DKD-PC12 cells. Fig. S5 shows the role of sytaxin-1A in the SNARE complex formation using BoNT/E-LC.

References

Baker, R.W., P.D. Jeffrey, M. Zick, B.P. Phillips, W.T. Wickner, and F.M. Hughson. 2015. A direct role for the Sec1/Munc18-family protein Vps33 as a template for SNARE assembly. *Science.* 349:1111–1114. http://dx.doi.org/10.1126/science.aac7906

Burkhardt, P., D.A. Hattendorf, W.I. Weis, and D. Fasshauer. 2008. Munc18a controls SNARE assembly through its interaction with the syntaxin N-peptide. *EMBO J.* 27:923–933. http://dx.doi.org/10.1038/emboj.2008.37

Choquet, D., and A. Triller. 2013. The dynamic synapse. *Neuron.* 80:691–703. http://dx.doi.org/10.1016/j.neuron.2013.10.013

Constals, A., A.C. Penn, B. Compans, E. Toulmé, A. Phillipat, S. Marais, N. Retailleau, A.S. Hafner, F. Coussen, E. Hosy, and D. Choquet. 2015. Glutamate-induced AMPA receptor desensitization increases their mobility and modulates short-term plasticity through unbinding from Stargazin. *Neuron.* 85:787–803. http://dx.doi.org/10.1016/j.neuron.2015.01.012

Dempsey, G.T., J.C. Vaughan, K.H. Chen, M. Bates, and X. Zhuang. 2011. Evaluation of fluorophores for optimal performance in localization-based super-resolution imaging. *Nat. Methods.* 8:1027–1036. http://dx.doi.org/10.1038/nmeth.1768

Fasshauer, D., and M. Margittai. 2004. A transient N-terminal interaction of SNAP-25 and syntaxin nucleates SNARE assembly. *J. Biol. Chem.* 279:7613–7621. http://dx.doi.org/10.1074/jbc.M312064200

Faul, F., E. Erdfelder, A. Buchner, and A.G. Lang. 2009. Statistical power analyses using G*Power 3.1: Tests for correlation and regression analyses. *Behav. Res. Methods.* 41:1149–1160. http://dx.doi.org/10.3758/BRM.41.4.1149

Gerber, S.H., J.C. Rah, S.W. Min, X. Liu, H. de Wit, I. Dulubova, A.C. Meyer, J. Rizo, M. Arancillo, R.E. Hammer, et al. 2008. Conformational switch of syntaxin-1 controls synaptic vesicle fusion. *Science.* 321:1507–1510. http://dx.doi.org/10.1126/science.1163174

Giannone, G., E. Hosy, F. Levet, A. Constals, K. Schulze, A.I. Sobolevsky, M.P. Rosconi, E. Gouaux, R. Tampé, D. Choquet, and L. Cognet. 2010. Dynamic superresolution imaging of endogenous proteins on living cells at ultra-high density. *Biophys. J.* 99:1303–1310. http://dx.doi.org/10.1016/j.bpj.2010.06.005

Greitzer-Antes, D., N. Barak-Broner, S. Berlin, Y. Oron, D. Chikvashvili, and I. Lotan. 2013. Tracking Ca²⁺-dependent and Ca²⁺-independent conformational transitions in syntaxin 1A during exocytosis in neuroendocrine cells. *J. Cell Sci.* 126:2914–2923. http://dx.doi.org/10.1242/jcs.124743

Han, G.A., N.R. Bin, S.Y. Kang, L. Han, and S. Sugita. 2013. Domain 3a of Munc18-1 plays a crucial role at the priming stage of exocytosis. *J. Cell Sci.* 126:2361–2371. http://dx.doi.org/10.1242/jcs.126862

Han, L., T. Jiang, G.A. Han, N.T. Malintan, L. Xie, L. Wang, F.W. Tse, H.Y. Gaisano, B.M. Collins, F.A. Meunier, and S. Sugita. 2009. Rescue of Munc18-1 and -2 double knockdown reveals the essential functions of interaction between Munc18 and closed syntaxin in PC12 cells. *Mol. Biol. Cell.* 20:4962–4975. http://dx.doi.org/10.1091/mbc.E09-08-0712

Harper, C.B., A. Papadopulos, S. Martin, D.R. Matthews, G.P. Morgan, T.H. Nguyen, T. Wang, D. Nair, D. Choquet, and F.A. Meunier. 2016. Botulinum neurotoxin type-A enters a non-recycling pool of synaptic vesicles. *Sci. Rep.* 6:19654. http://dx.doi.org/10.1038/srep1965426805017

Hayashi, T., H. McMahon, S. Yamasaki, T. Binz, Y. Hata, T.C. Südhof, and H. Niemann. 1994. Synaptic vesicle membrane fusion complex: action of clostridial neurotoxins on assembly. *EMBO J.* 13:5051–5061.

Heilemann, M., S. van de Linde, M. Schüttpelz, R. Kasper, B. Seefeldt, A. Mukherjee, P. Tinnefeld, and M. Sauer. 2008. Subdiffraction-resolution fluorescence imaging with conventional fluorescent probes. *Angew. Chem. Int. Ed. Engl.* 47:6172–6176. http://dx.doi.org/10.1002/anie.200802376

Hu, S.H., M.P. Christie, N.J. Saez, C.F. Latham, R. Jarrott, L.H. Lua, B.M. Collins, and J.L. Martin. 2011. Possible roles for Munc18-1 domain 3a and Syntaxin1 N-peptide and C-terminal anchor in SNARE complex formation. *Proc. Natl. Acad. Sci. USA.* 108:1040–1045. http://dx.doi.org/10.1073/pnas.0914906108

Izeddin, I., J. Boulanger, V. Racine, C.G. Specht, A. Kechkar, D. Nair, A. Triller, D. Choquet, M. Dahan, and J.B. Sibarita. 2012. Wavelet analysis for

single molecule localization microscopy. *Opt. Express.* 20:2081–2095. http://dx.doi.org/10.1364/OE.20.002081

Kavanagh, D.M., A.M. Smyth, K.J. Martin, A. Dun, E.R. Brown, S. Gordon, K.J. Smillie, L.H. Chamberlain, R.S. Wilson, L. Yang, et al. 2014. A molecular toggle after exocytosis sequesters the presynaptic syntaxin1a molecules involved in prior vesicle fusion. *Nat. Commun.* 5:5774. http://dx.doi.org/10.1038/ncomms6774

Kubala, M.H., O. Kovtun, K. Alexandrov, and B.M. Collins. 2010. Structural and thermodynamic analysis of the GFP:GFP-nanobody complex. *Protein Sci.* 19:2389–2401. http://dx.doi.org/10.1002/pro.519

Kusumi, A., T.A. Tsunoyama, K.M. Hirosawa, R.S. Kasai, and T.K. Fujiwara. 2014. Tracking single molecules at work in living cells. *Nat. Chem. Biol.* 10:524–532. http://dx.doi.org/10.1038/nchembio.1558

Lang, T., D. Bruns, D. Wenzel, D. Riedel, P. Holroyd, C. Thiele, and R. Jahn. 2001. SNAREs are concentrated in cholesterol-dependent clusters that define docking and fusion sites for exocytosis. *EMBO J.* 20:2202–2213. http://dx.doi.org/10.1093/emboj/20.9.2202

Malintan, N.T., T.H. Nguyen, L. Han, C.F. Latham, S.L. Osborne, P.J. Wen, S.J. Lim, S. Sugita, B.M. Collins, and F.A. Meunier. 2009. Abrogating Munc18-1-SNARE complex interaction has limited impact on exocytosis in PC12 cells. *J. Biol. Chem.* 284:21637–21646. http://dx.doi.org/10.1074/jbc.M109.013508

Manley, S., J.M. Gillette, G.H. Patterson, H. Shroff, H.F. Hess, E. Betzig, and J. Lippincott-Schwartz. 2008. High-density mapping of single-molecule trajectories with photoactivated localization microscopy. *Nat. Methods.* 5:155–157. http://dx.doi.org/10.1038/nmeth.1176

Martin, S., V.M. Tomatis, A. Papadopulos, M.P. Christie, N.T. Malintan, R.S. Gormal, S. Sugita, J.L. Martin, B.M. Collins, and F.A. Meunier. 2013. The Munc18-1 domain 3a loop is essential for neuroexocytosis but not for syntaxin-1A transport to the plasma membrane. *J. Cell Sci.* 126:2353–2360. http://dx.doi.org/10.1242/jcs.126813

Maucort, G., R. Kasula, A. Papadopulos, T.A. Nieminen, H. Rubinsztein-Dunlop, and F.A. Meunier. 2014. Mapping organelle motion reveals a vesicular conveyor belt spatially replenishing secretory vesicles in stimulated chromaffin cells. *PLoS One.* 9:e87242. http://dx.doi.org/10.1371/journal.pone.0087242

Misura, K.M., R.H. Scheller, and W.I. Weis. 2000. Three-dimensional structure of the neuronal-Sec1-syntaxin 1a complex. *Nature.* 404:355–362. http://dx.doi.org/10.1038/35006120

Nair, D., E. Hosy, J.D. Petersen, A. Constals, G. Giannone, D. Choquet, and J.B. Sibarita. 2013. Super-resolution imaging reveals that AMPA receptors inside synapses are dynamically organized in nanodomains regulated by PSD95. *J. Neurosci.* 33:13204–13224. http://dx.doi.org/10.1523/JNEUROSCI.2381-12.2013

Papadopulos, A., G.A. Gomez, S. Martin, J. Jackson, R.S. Gormal, D.J. Keating, A.S. Yap, and F.A. Meunier. 2015. Activity-driven relaxation of the cortical actomyosin II network synchronizes Munc18-1-dependent neurosecretory vesicle docking. *Nat. Commun.* 6:6297. http://dx.doi.org/10.1038/ncomms7297

Parisotto, D., M. Pfau, A. Scheutzow, K. Wild, M.P. Mayer, J. Malsam, I. Sinning, and T.H. Söllner. 2014. An extended helical conformation in domain 3a of Munc18-1 provides a template for SNARE (soluble *N*-ethylmaleimide-sensitive factor attachment protein receptor) complex assembly. *J. Biol. Chem.* 289:9639–9650. http://dx.doi.org/10.1074/jbc.M113.514273

Rickman, C., D.A. Archer, F.A. Meunier, M. Craxton, M. Fukuda, R.D. Burgoyne, and B. Davletov. 2004. Synaptotagmin interaction with the syntaxin/SNAP-25 dimer is mediated by an evolutionarily conserved motif and is sensitive to inositol hexakisphosphate. *J. Biol. Chem.* 279:12574–12579. http://dx.doi.org/10.1074/jbc.M310710200

Rickman, C., C.N. Medine, A. Bergmann, and R.R. Duncan. 2007. Functionally and spatially distinct modes of munc18-syntaxin 1 interaction. *J. Biol. Chem.* 282:12097–12103. http://dx.doi.org/10.1074/jbc.M700227200

Saxton, M.J. 1993. Lateral diffusion in an archipelago. Single-particle diffusion. *Biophys. J.* 64:1766–1780. http://dx.doi.org/10.1016/S0006-3495(93)81548-0

Saxton, M.J., and K. Jacobson. 1997. Single-particle tracking: Applications to membrane dynamics. *Annu. Rev. Biophys. Biomol. Struct.* 26:373–399. http://dx.doi.org/10.1146/annurev.biophys.26.1.373

Schiavo, G., A. Santucci, B.R. Dasgupta, P.P. Mehta, J. Jontes, F. Benfenati, M.C. Wilson, and C. Montecucco. 1993. Botulinum neurotoxins serotypes A and E cleave SNAP-25 at distinct COOH-terminal peptide bonds. *FEBS Lett.* 335:99–103. http://dx.doi.org/10.1016/0014-5793(93)80448-4

Sengupta, P., T. Jovanovic-Talisman, D. Skoko, M. Renz, S.L. Veatch, and J. Lippincott-Schwartz. 2011. Probing protein heterogeneity in the plasma membrane using PALM and pair correlation analysis. *Nat. Methods.* 8:969–975. http://dx.doi.org/10.1038/nmeth.1704

Smyth, A.M., L. Yang, K.J. Martin, C. Hamilton, W. Lu, M.A. Cousin, C. Rickman, and R.R. Duncan. 2013. Munc18-1 protein molecules move between membrane molecular depots distinct from vesicle docking sites. *J. Biol. Chem.* 288:5102–5113. http://dx.doi.org/10.1074/jbc.M112.407585

Toonen, R.F., O. Kochubey, H. de Wit, A. Gulyas-Kovacs, B. Konijnenburg, J.B. Sørensen, J. Klingauf, and M. Verhage. 2006. Dissecting docking and tethering of secretory vesicles at the target membrane. *EMBO J.* 25:3725–3737. http://dx.doi.org/10.1038/sj.emboj.7601256

Trimble, W.S., and S. Grinstein. 2015. Barriers to the free diffusion of proteins and lipids in the plasma membrane. *J. Cell Biol.* 208:259–271. http://dx.doi.org/10.1083/jcb.201410071

Vaidyanathan, V.V., K. Yoshino, M. Jahnz, C. Dörries, S. Bade, S. Nauenburg, H. Niemann, and T. Binz. 1999. Proteolysis of SNAP-25 isoforms by botulinum neurotoxin types A, C, and E: Domains and amino acid residues controlling the formation of enzyme-substrate complexes and cleavage. *J. Neurochem.* 72:327–337. http://dx.doi.org/10.1046/j.1471-4159.1999.0720327.x

van de Linde, S., A. Löschberger, T. Klein, M. Heidbreder, S. Wolter, M. Heilemann, and M. Sauer. 2011. Direct stochastic optical reconstruction microscopy with standard fluorescent probes. *Nat. Protoc.* 6:991–1009. http://dx.doi.org/10.1038/nprot.2011.336

van den Bogaart, G., T. Lang, and R. Jahn. 2013. Microdomains of SNARE proteins in the plasma membrane. *Curr. Top. Membr.* 72:193–230. http://dx.doi.org/10.1016/B978-0-12-417027-8.00006-4

Veatch, S.L., B.B. Machta, S.A. Shelby, E.N. Chiang, D.A. Holowka, and B.A. Baird. 2012. Correlation functions quantify super-resolution images and estimate apparent clustering due to over-counting. *PLoS One.* 7:e31457. http://dx.doi.org/10.1371/journal.pone.0031457

Verhage, M., A.S. Maia, J.J. Plomp, A.B. Brussaard, J.H. Heeroma, H. Vermeer, R.F. Toonen, R.E. Hammer, T.K. van den Berg, M. Missler, et al. 2000. Synaptic assembly of the brain in the absence of neurotransmitter secretion. *Science.* 287:864–869. http://dx.doi.org/10.1126/science.287.5454.864

Voets, T., R.F. Toonen, E.C. Brian, H. de Wit, T. Moser, J. Rettig, T.C. Südhof, E. Neher, and M. Verhage. 2001. Munc18-1 promotes large dense-core vesicle docking. *Neuron.* 31:581–591. http://dx.doi.org/10.1016/S0896-6273(01)00391-9

Zilly, F.E., N.D. Halemani, D. Walrafen, L. Spitta, A. Schreiber, R. Jahn, and T. Lang. 2011. Ca^{2+} induces clustering of membrane proteins in the plasma membrane via electrostatic interactions. *EMBO J.* 30:1209–1220. http://dx.doi.org/10.1038/emboj.2011.53